Paramagnetism found in Mn-doped CuO nanofibers at room temperature explained by XPS, XAS, and Rietveld method

M. Piñon-Espitia[a,*], A. Duarte-Möller[b,⋆], S. Verdugo-Miranda[b], B. López-Walle[c] and M. T. Ochoa-Lara[a]

[a]*Centro de Investigación en Materiales Avanzados, S.C., Physics Departament., Miguel de Cervantes 120, Chihuahua 31136, Chihuahua, México,*
[*]*e-mail: manuel.pinon@cimav.edu.mx*
[b]*Departamento de Física, Matemáticas e Ingeniería. Universidad de Sonora, Unidad Regional Sur. Lázaro Cárdenas del Río 100, Francisco Villa, 85880, Navojoa, Son. México.*
[⋆]*e-mail: josealberto.duarte@unison.mx*
[c]*Universidad Autónoma de Nuevo León, Fac. de Ingeniería Mecánica y Eléctrica, Av. Universidad S/N, Cd. Universidatia, San Nicolás de los Garza, Nuevo León, 66450, México.*

Received 1 February 2024; accepted 27 May 2024

CuO and 3% Mn-doped CuO nanofibers were synthesized employing the electrospinning method. X-ray diffraction (XRD) verified a monoclinic phase with a C 2/c space group. An electronic density analysis, obtained using Fullprof software, was projected on the (110) and (001) planes for both materials, showing modifications in the Cu positions. This fact generated vacancies involved in the paramagnetism formation in the Mn-doped CuO nanofibers, in contrast to the mixed magnetic phase composed by both ferromagnetic and paramagnetic behaviors found in the undoped CuO. The vacancy amount was quantified by X-ray absorption spectroscopy (XAS) applying CASTEP software. In addition, an analysis from Cu 2p XPS peaks supports the predicted Cu-Cu rearrangement by the Fullprof software study, while the presence of Cu^{1+} confirms the substitution of Mn for Cu in the doped sample.

Keywords: Nanofibers; CuO; Mn-doped; XPS; electron density; XAS.

DOI: https://doi.org/10.31349/RevMexFis.70.051002

1. Introduction

CuO is a well-known p-type semiconductor with a narrow band-gap ranging from 1.27 to 2.1eV. It has a tenorite phase (C_{2h}^6 (C2/c) space group) that includes octahedral sites, arising from the coordination of Cu atom with four atoms of O [1,2]. In addition to its large surface area-to-volume ratio, nanometric CuO is known for its excellent electronic, optoelectronic, magnetic, catalytic, electrochemical, and photovoltaic properties. These qualities facilitate its use in various applications, including semiconductor oxide sensors, optoelectronic devices, catalysis, and superconductors [3].

The 1D CuO structures have been synthesized and studied especially in different nanostructures such as nanowires, nanobelts, nanotubes, nanoribbons, nanorods, nanoflakes, nanoflowers and nanofibers [6]. In particular, CuO nanofibers have been analyzed in several studies, because their properties related to its nanodimension [1-7]. The nanofiber synthesis has been performed by several methods: wet chemical, thermal oxidation, electrochemical deposition, electrospinning. The last one stands out due to the easy preparation method, efficiency and low-cost fabrication [2,3].

The magnetic properties of Doped CuO can differ from those observed in the un-doped CuO material, as can be shown through the detected magnetic phases, at room temperature: a superparamagnetism in CuO nanoparticles [9-14] or paramagnetism in Mn doped CuO nanoparticles [12,15].

The Full-prof suite allows to predict properties such as: particle shape and size, de-formation, magnetic structure, crystalline structure, XRD refinement, among others. The crystalline structure calculation is very relevant because will allow us to get the electron density, useful to know the position evolution of the atoms due to the Mn doping. This results support that the position modifications predicted agree with the paramagnetic be-havior in exhibited in the Mn doped fibers.

We reported [6,7] information contained in Cu 2p and O 1s orbitals of CuO, analyzed and quantified by XPS technique. Specially, these pikes displayed a magnetic behavior, through their deformation. These results agrees with those reported by [9]. In addition, in Refs. [6,7,12] was shown the presence of vacancies and hole (shake-up), whose effects generate a structural deformation (Jahn-Teller effect) [4-8].

Paramagnetism is characterized by the orientation of spins in relation to an applied magnetic field, both of which are small and positive in magnitude. These magnetic properties have been investigated in CuO, which exhibits a ferromagnetic behavior of approx-imately 2×10^{-2} emu/g [5-7] and an antiferromagnetic phase between 230 K and 215 K [5-7]. Furthermore, the susceptibility studies cited in references [5-7] indicate that with a de-crease in particle size, the antiferromagnetic (AFM) phase is absent. This phenomenon is associated with the ellipsoidal shape of the particles, as described by the author in their study [6].

The aim of this work is to support our previous study of paramagnetism [12] with new information on the 3% Mn-

doped CuO nanofibers using the results predicted by the Fullprof here, about the modifications of the interatomic distances in the structure, obtained from the determined atom density. In addition, from XPS results of Borci *et al* [9], corroborated by us [6,7], the paramagnetic phase observed in these references, can be explained too through the information obtained from the VO quantification taken from CuO O 1s pike analysis and completed with the chemical coordination obtained from XPS Cu 2p orbital.

2. Materials and methods

2.1. Nanofiber synthesis

Preparation of solutions

The reagents employed for the CuO nanofiber synthesis were: copper (II) acetate monohydrate (Merk, 99.99 trace metal basis), distilled water, Polyvinyl Alcohol (PVA, Sigma Aldrich, 180,000 W) and Manganese (II) acetate tetrahydrate (Merk, ACS $> 98\%$).

The polymeric undoped CuO nanofibers (A-NFs) were prepared by adding a solution containing 1 g of copper acetate, previously diluted in distilled water, to other containing 20 g of an aqueous 8% PVA solution (after 24 h of 100 rpm of agitation at 100°C).

The 3% Mn-doped CuO nanofibers (B-NFs) were obtained, by adding 0.003 g to the previously prepared solution. The final solutions required an agitation of 100 rpm for 24 h at 50°C.

Electrospinning method

Ten ml of the undoped solution were loaded in a syringe with a # 22 needle. It was placed in the electrospinning standard equipment (Tong Li Tech) at 20 cm from an aluminum plate, used as the fiber collector, applying an electric field of 8 kV, at a flow rate of 0.3 ml/h.

The BNFs were synthesized with the same method only exchanging the solution for the 3% Mn-doped solution.

TGA-DSC technique

Through TGA-DSC technique, using the SDT-TGA Q600 (TA Instruments) equipment, the burn temperature was measured for both polymeric A-NFs and B-NFs samples.

The experimental conditions were 10 °C/min rate, with a $25 - 1000$°C temperature range.

Semiconductor nanofiber synthesis

After the DSC-TGA test, the chosen muffle temperature to synthesize the CuO and Mn-doped nanofibers, was 700°C, during 4 hours, with a ramp of 3°C per minute.

2.2. Characterization

2.2.1. *XRD, Fullprof and VESTA*

The structural characterization was performed on the X'Pert Pro diffractometer equipped with a X'Celetator detector, using Cu Kα radiation (1.5418 Å). The XRD patterns were taken from $2\theta = 30°$ to 65° with an 0.05 s^{-1} step.

The XRD spectra were determined considering the multivalent states, reported for the Rietveld method, in previous publications [1,12].

The lattice parameters obtained from the experimental XRD spectra were used for the refinement process by applying the Fullprof [22] with a Pseudo-Voight peak (least squares method) assigned. A CIF structure was obtained and combined with the VESTA software results [23]. Then, the 2-D and 3-D electron density was calculated. The crystalline structure thermal factor determined by S Arbrik, *et al*, 1970 was considered to model the structures of the synthesized materials [24].

2.2.2. *SEM*

To confirm the polymeric nature of the electrospun nanofibers, morphology images for both A-NFs and B-NFs samples were acquired using Hitachi SU3500 SEM equipment. A 1 cm^2 square-shaped aluminum fragment, collected from the fiber collector, was utilized for imaging.

2.2.3. *TEM, EDS, JImage*

Through dispersion method, TEM samples of A-NFs and B-NFs were prepared on 3 mm diameter grids to observe their morphology with a Hitachi 7700 TEM. Additionally, to confirm the presence of Cu, O, and Mn, an EDS analysis was conducted.

The diameter of the nanofibers was averaged using JImage software [26] for both A-NFs and B-NFs samples. The results were displayed in histograms, fitted with a log-normal function, using Origin Pro8.6 software [16].

2.2.4. *XPS*

Previous XPS studies performed by our team [6, 7], employed a Thermoscience Fisher Escalab Xi equipment. The process conditions and analysis methods used are detailed in the referenced studies.

2.2.5. *Magnetic susceptibility analysis*

0.02 g of A-NFs and B-NFs were placed in a sample holder of the magnetometer. The diamagnetic susceptibility value of the sample holder, measured as (-2.30×10^{-8} emu/Oe). Magnetic measurements were conducted using a commercial superconducting quan-tum inference device (SQUID) magnetometer at a temperature of 300 K. Hysteresis loops were obtained by applying a magnetic field H within the range of

-80 kOe $\leq$ H $\geq$ 80 kOe. Magnetic susceptibility was calculated from 2 K to 300 K using the Curie-Weiss equation.

$$M = C\left(\frac{B}{T}\right). \quad (1)$$

In this equation, M represents the magnetization, B the applied magnetic field in kiloOersteds (kOe), T the temperature in Kelvin K, and C the Curie constant. Consequently, the graph depicting the inverse of the susceptibility is expressed as $1/C$.

2.2.6. Computational methods: CASTEP, XAS

For both A-NFs and B-NFs superlattice samples, a complementary ab initio XAS analysis was conducted using the Cambridge Sequential Total Energy Package (CASTEP). This involved applying density functional theory (DFT) and the ultrasoft pseudopotential plane-wave (PP-PW) methodology.

As CuO is an antiferromagnetic (AFM) oxide, a Hubbard potential of 7.5 eV was chosen for constructing three crystal structures: a CuO lattice, a 3% Mn-doped CuO superlattice, and a CuO superlattice containing only V_O. These were modeled within a $2 \times 2 \times 1$ supercell, occupying the octahedral (O_h) coordination sites.

The chemical coordination between the oxygen and copper atoms was calculated from these structures, optimizing them, by applying the next conditions: a convergence tolerance of fine quality, energy of 1×10^{-5} Ha, Max, force of 0.002 Ha/Å, a Max., displacement of 0.005Å, a maximum of 50 iterations and Max. Step size of 0.3Å. Moreover, their energy was calculated to obtain only the O 1 s orbital spectrum of both CuO structures. In addition, a separation of 1 nm was maintained between core-hole atoms. Finally, the supplementary conditions, a cutoff energy of 550 eV, pseudopotentials on the fly, an energy range of 0-50 eV and a k-point set: $10 \times 10 \times 10$, were considered.

To research the presence of V_O into the supercell with $2 \times 2 \times 1$ size and octahedral (O_h) arrangement configuration was built. We proceeded to optimize these structures using a convergence tolerance of fine quality, an energy of 1×10^{-5}Ha, Max, force of 0.002 Ha/Å and a Max. Displacement of 0.005Å, maximum iterations of 50 and a step size of 0.3Å. After the structures were optimized obtaining their energies to calculate the spectroscopic properties of the O 1 s spectra, maintaining a separation of 1 nm between core-hole atoms.

To correlate the energy of the XAS spectra corresponding to the experimental XPS spectra (6,7), theorical transition energy (E_{TE}), was applied. This energy the result of the valence state energy difference ($\Delta E_{\text{valence}}$) plus the contribution for the core orbitals ($\Delta E_{\text{core(atom)}}$). In addition, the excited states of all orbitals and the core hole correction were considered. The resultant data were introduced in the Eqs. (1) and (2) to the determine the final energy of the spectra [17]. The origin of these data is CASTEP calculation sheets.

The O 1 s experimental spectra fitting was performed in agree (6,7) reference. The deconvolution of XAS spectra was calculated by Origin Pro8.6 software [16].

3. Results and discussions

3.1. XRD analysis by Fullprof

Experimental XRD of A-NFs and B-NFs are displayed in Fig. 1a)-1b) (black dots), showing the presence of Tenorite structure, for both samples, corroborated by the PDF 80-1268 (Power Diffraction File), in Fig.1c). The Fig. 1a), 1b) includes the calculated XRD from Rietveld refinement (red line) for both samples, that agrees with the experimental XRD. The displacements on 2θ axis to the left in B-NFs XRD spectrum with respect to that of the A-NFs were observed, indicating deformations due to generated compressions by the doping.

Microdeformations of 13.0125×10^{-4} in size for A-NFs and 15.8862×10^{-4} in size for B-NFs were predicted by Fullprof fit, and the dislocation density calculated as 2.5×10^{-3} nm^{-2} for the A-NFs and 4.526×10^{-4} nm^{-2} for the B-NFs. The respective particle size averages were 22 nm for the A-NFs sample and 43 nm for B-NFs, which in agree with those previously reported [14].

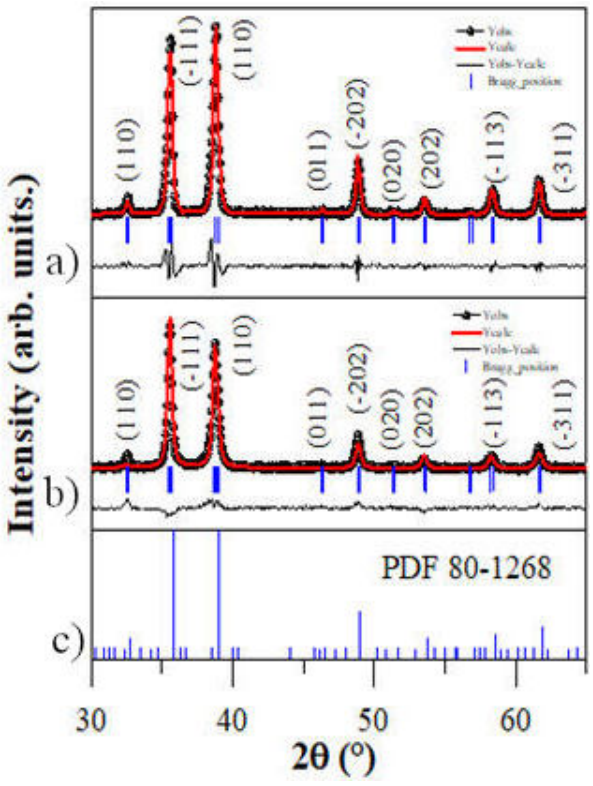

FIGURE 1. a) Experimental (black dots) and calculated by Fullprof suite XRD (red line) for A-NFs, b) experimental (black dots) and calculated by software XRD (red line) for B-NFs and c) Tenorite phase PDF chart 80-1268 (Power Diffraction File).

TABLE I. Lattice parameters of the study NFs compared to bulk CuO (Sigma Aldrich, 99.9% purity). Additionally, the table displays the variation of the O^2 ion β, cell volume V and the standard deviation of the experimental-calculated fit (χ^2).

Structure	Lattice parameters			Y	β(Å°)	V(Å^3)	χ^2
	a(Å)	b(Å)	c(Å)				
Bulk	4.6837	3.4226	5.1288	0.4188	99.54	81.19	-
A-NFs	4.6807	3.4227	5.1274	0.4158	99.409	81.039	1.44
B-NFs	4.68715	3.4245	5.1327	0.4467	99.461	81.265	1.33

The Table I shows the relative shifts due to the Rietveld refinement fittings for each XRD spectrum. A greater variation of lattice parameters can be detected in the B-NFs, while the A-NFs variation is similar to that observed in the bulk material. This variation allows elucidating changes in their crystal structure with respect to the average crystallite size, defects in their structure related to doping and changes in the O^{2-} "y" anion position. The variation of the oxygen "y" positions in the synthesized materials show shrinkage shifts, whichs affect the chemical coordination [1,20,21]. Likewise, the β (°) parameter exhibits angular distortion in the structure (Jahn-Teller effect).

According to S. Asbrink, *et al*., 1970, J. Ghijsen, *et al*., 1988 and J. I. Langford, *et al*., 1991, the variations obtained for the lattice parameters are mainly due to the oxide non-stoichiometry expressed as $Cu_{1-x}O$, where "x" that depends on the physicochemical conditions of oxide preparation. This condition would mean variations of interatomic distances and nearest-neighbor distances [16,25,26]. The parameter "y" (atomic position of the O_2- anion) shows variability in the NFs being it higher for the Mn-doped material.

We can see that the volume in the A-NFs was contracted and in the B-NFs was expanded with respect to the bulk sample, due to the substitution of Mn^{2+} (0.66Å) for Cu^{2+} (0.54Å) into the structure. In conjunction with the variations of the lattice parameters and the "y" parameter a lattice deformation was generated due to the decrease in crystallite size, in this respect A. Khorsand Zak, *et al.*, 2011 reported that the 2θ shift is a consequence of presence of dislocations in the crystallite. Finally, the obtained values of the standard deviation $\chi^2 > 1$ corroborated the crystallite size decrease in nanometer materials reported in Refs. [31-35].

TABLE II. Cation and anion behavior into the Tenorite structure of the A-NFs and B-NFs.

Sample	Bond length (Cu-O) (Å)	Med (Cu-O) (e/Å^3)	Bond length (Cu-Cu) (Å)	Med (Cu-Cu) (e/Å^3)
A-NFs	2.8993 (3)	0.2174	1.9560 (4)	0.0994
B-NFs	2.4216 (16)	0.1918	1.8240 (18)	0.2559

Note: MED (Measure Electronic Density)

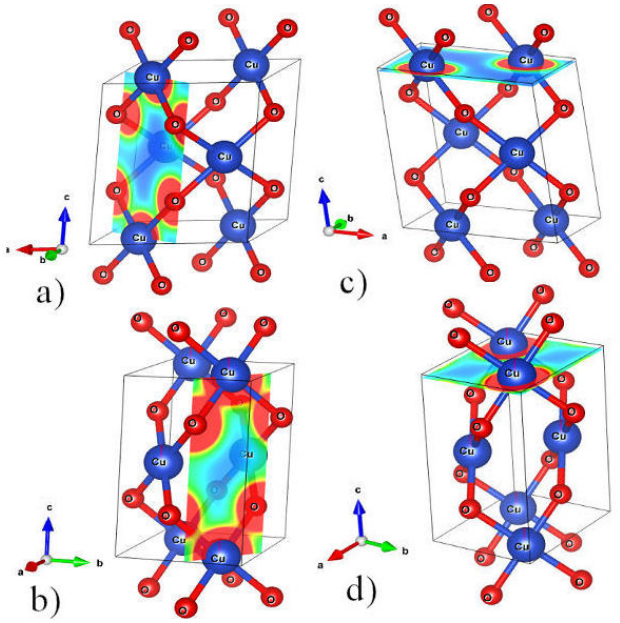

FIGURE 2. 3-D crystal structures obtained and configured for (110) and (001) planes by VESTA, for. A-NFs shown in a) and c), and for B-NFs in b) and d).

3.1.1. *Electron density in the tenorite structure*

The structures ANFs and BNFs in the (110) and (001) planes were obtained by Rietveld refinement, are displayed in Fig. 2a) and 2c) illustrate the A-NFs projections for both planes, while Fig. 2b) and 2d) correspond to those of the B-NFs.

Figure 3c), and 3d), depict the electron densities for A-NFs and B-NFs on the (001) plane, highlighting the shorter distances among Cu atoms in B-NFs compared to those in A-NFs, on this plane (see Table II).

The Fig. 3a) and 3b) in the (110) plane exhibit the atomic distribution in both samples, showing for the neighboring atoms Cu and O, a charge transfer curve, characterized by a strain of the electron density with a peanut shape, shown in Fig. 3a) and 3c). The distance decreasing among the Cu atoms observed in the B-NFs (001) plane, is a result of doping, associated to a paramagnetic behavior by Hongwei Qin, *et al.*, 2010, through Cu 2*p* XPS doublets [1,13,14], attributed to the crystallographic orientation by R.A. Borzi, *et al*., 2001,

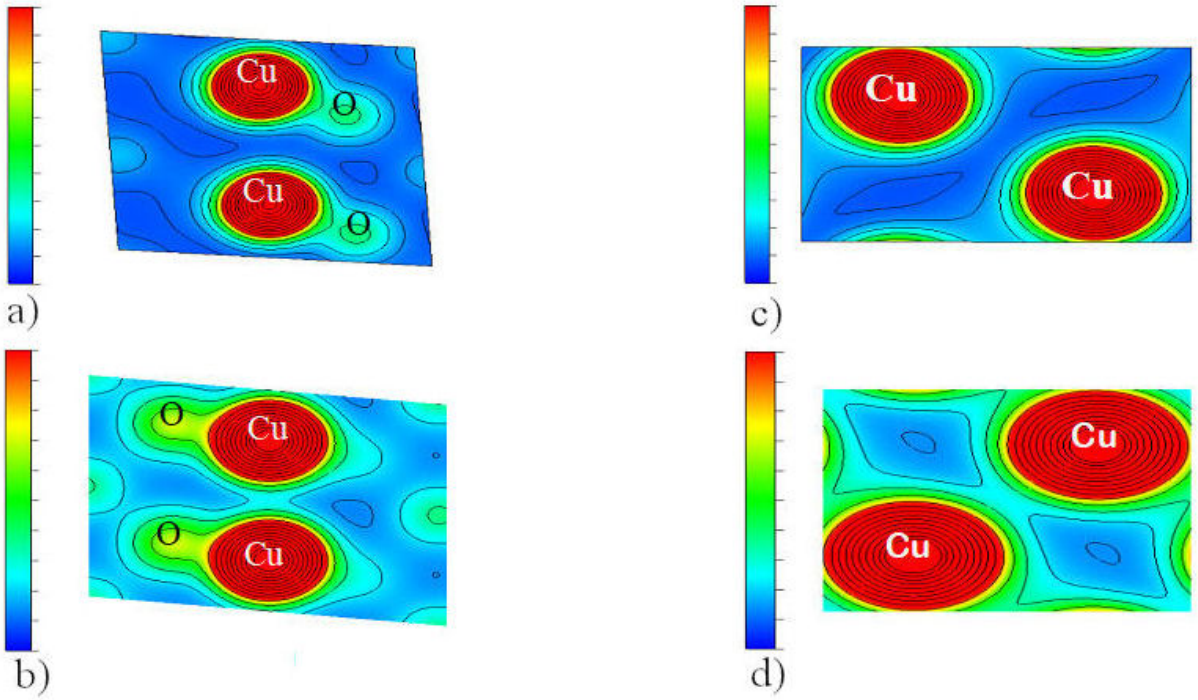

FIGURE 3. 2-D electron density for the (001) y (110) planes, for a) and b) A-NFs, and c) and d) for B-NFs.

who supports the same idea about the presence of paramagnetism, in base to energy difference measures between CuO2*p* doublets, in the (001) plane [13,14]. From the Table II, we can observe that the calculated Cu-O distances at the (110) plane, by the Fullprof are smaller for the doped material, discussed above for the A-NFs. The same decreasing effect happens for the B-NFs in the (110) plane. Both results agree with those of the other authors. The electron density is different for each plane and for both samples, fact attributed to different planes and doping.

A comparison between A-NFs and B-NFs chemical bonding is shown the Fig. 4 that allows to distinguish the interatomic distances between Cu^{2+} and O^{2-} ions, corresponding to the (110) and (001) planes. The binding energy according to in the (110) plane for A-NFs has an electron density of 0.2174 e/Å^3, and in the (001) plane 0.1050 e/Å^3. In the case of B-NFs, the (110) plane electron density shows an energy of 0.1918 e/Å^3, and in the (001) plane its electron density is 0.2623 e/Å^3. These NFs parameters are shown in Table II, compared with those of S. Asbrik and L.-J. Norrby, 1970 showed great similarity, between Cu-O distance for of the B-NFs and for the Cu-Cu distance for the A-NFs [19]. G. Herrera-Perez, *et al.*, 2022 propose a generated covalent bond from a hybridization, similar to Hanxing Cao, *et al.*, 2017 [29] result in a theoretical study of CuO, a covalent bond between O and Cu, was measured: 1.947Å^3. In the case of Fig. 4b) we can see that distance between the atoms increases and the covalence decreases, in the study of the cited author the distance between the same atoms suggests that the charge transfer increases -0.65 eV. These data suggest that there is a combination of electrovalent bonding (ionic bonding) and covalent bonding suggested by the authors [1,38].

3.2. SEM-TEM analysis

From the analysis of the Fig. 5a) and 5c) it can be observed the pure and doped polymeric fibers, where a diameter comparison shows an increase for the B-NFs, shown by the JImage Fig. 5b) and 5d). After the heat treatment applied at 700°C, the nanofibers are obtained and some fragments displayed in the TEM micrographs Fig. 5e) and 5f), whose diameter averages show a notable size increase for the B-NFs. This result corroborates that the Mn doping increases the fiber diameter, probably due to be bigger (0.80Å) than the copper (0.73Å) atom.

3.3. XPS Analysis

An oxidative evolution was detected from the XPS analysis of Cu 2*p* orbitals for A-NFs and B-NFs in their formation derived from the heat treatment and the presence of surface phenomena shown in reference [1,20]. In addition, in their multiplet structure it can be noted a crystalline symmetric distortion derived from size effects, microtensions and defects associated with the Cu^{2+} and O^{2-} vacancies [14]. From the multiplet structure calculations, the shape of Cu 2*p* primary peaks, after doping, is modified to characteristic shape linked with shifts in the spin-orbit coupling and with the chemical coordination.

The Cu 2*p* pike changes in the energy indicated [6,7] both the spin-orbit coupling and the chemical coordination

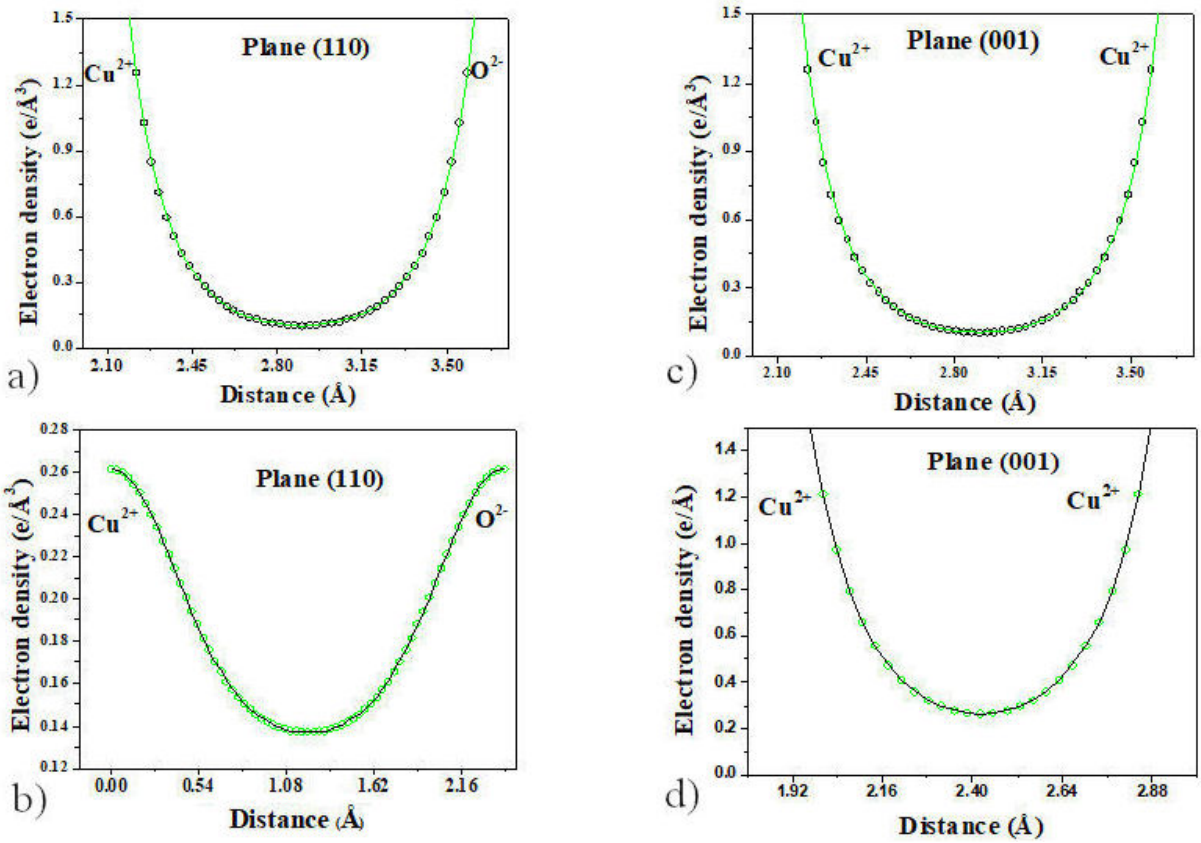

FIGURE 4. Electron density for A-NFs and B-NFs, in their respective (110) and (001) planes.

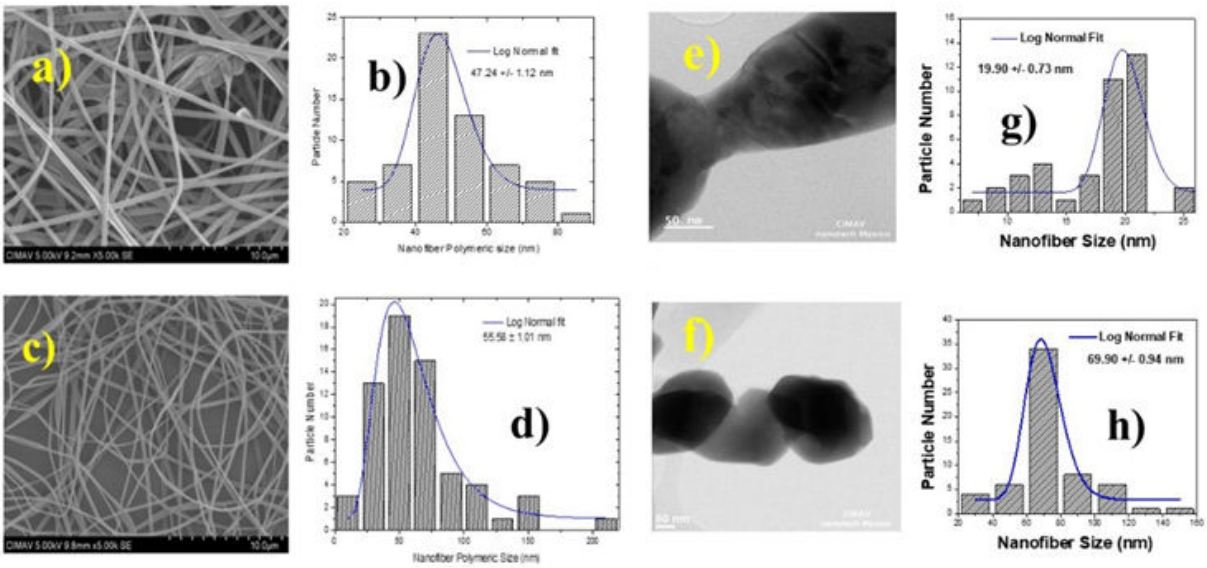

FIGURE 5. Electrospun and polymeric fibers: SEM images from a) A-NFs and c) B-NFs; b) and d) show the A-NFs and B-NFs diameter averages graphed by JImage software. In addition, e) and f) exhibit TEM micrographs of A-NFs and B-NFs fragments, respectively.

changes, in the Mn-doped material, mentioned above. A transformation from a structure with Oh sites to a one with tetrahedral sites is shown by the Cu 2*p* pike new shape, due to Jahn-Teller effect. In addition, The O-Cu-O in the A-NFs shows a high-spin ($3d^9$), generating a CuO more susceptible to present magnetic phenomena, shown by the charge transference calculation, performed by CTM4XAS [14], in contrast to B-NFs, O-Cu-O in Mn has an intrinsic property, $3d^4$ low spin generating less sensibility to magnetic behavior illustrated in Fig. 6 of Ref. [14].

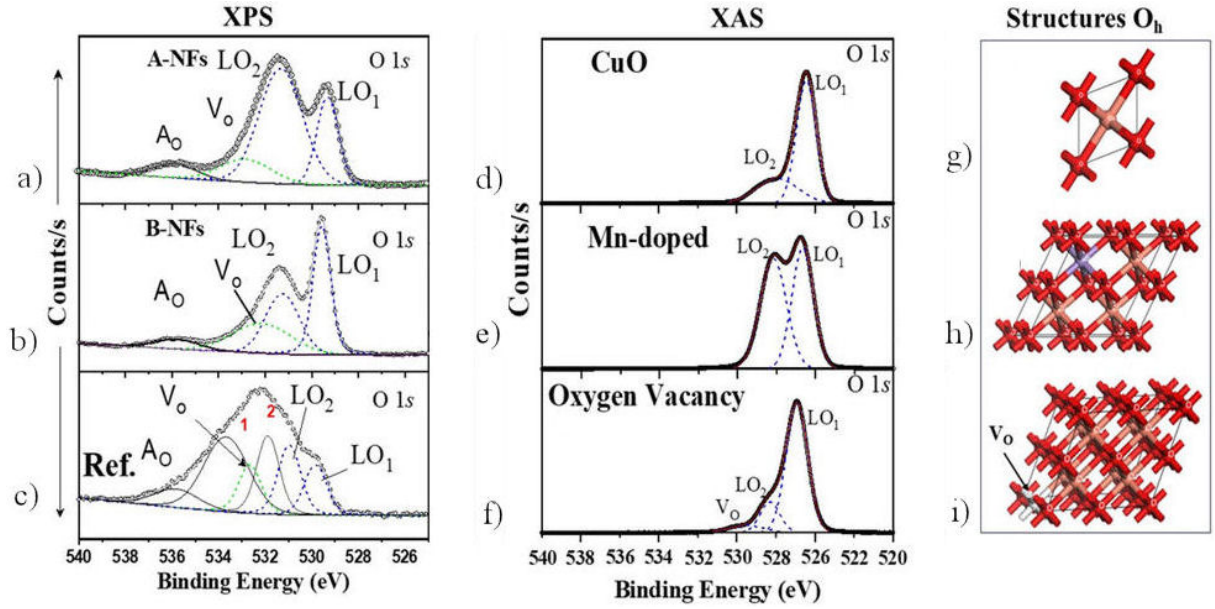

FIGURE 6. Comparative study on O 1s orbital, a) and b) experimental and c) reference. d), e) and f) panels show the O 1s orbitals calculated by CASTEP. Panels g), h), i) correspond to the Oh structures of: CuO, 3.0% Mn-doped CuO and CuO with VO, respectively.

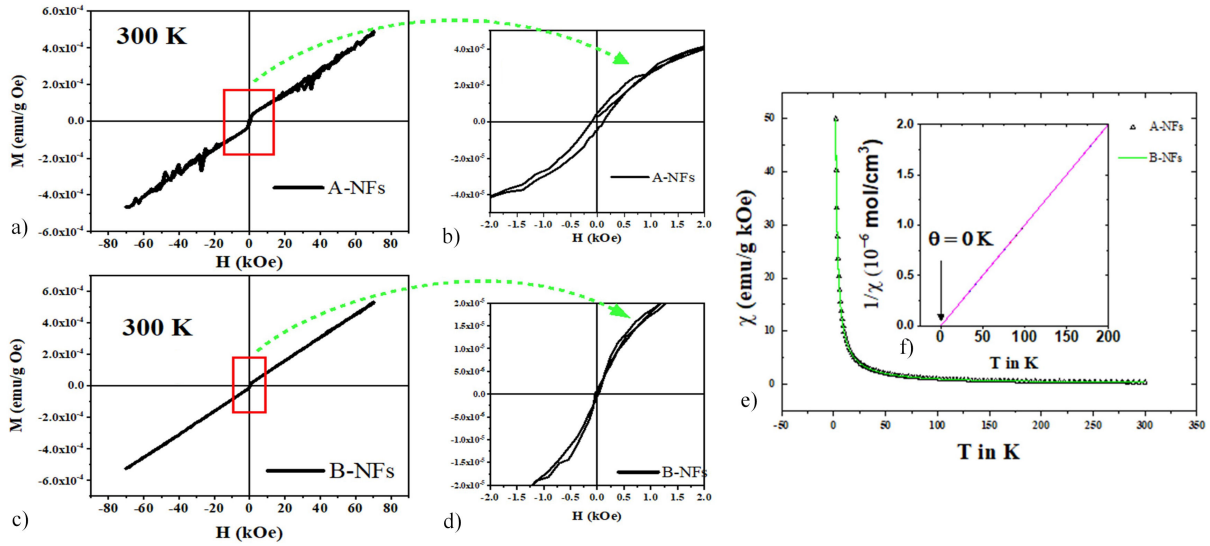

FIGURE 7. a)-b) and c)-d) displayed the magnetization $\vec{M}$ versus magnetic field ($\vec{H}$) response for A-NFs and B-NFs, respectively. The right panel presents two graphs; e) describes the AFM behavior of the studied NFs and panel f) illustrates the inverse of the susceptibility for both materials.

The Fig. 6a), 6b) and 6c) exhibits the XPS peaks of the O 1s orbitals for the A-NFs, B-NFs, and for the commercial sample, respectively and are compared with those of the theoretical reference structures Figs. 6g), 6h) and 6i). The modeled structure by CASTEP (XAS) of: CuO, 3 wt % Mn-doped CuO and CuO with 3% of $V_O$are exhibited in Fig. 6d), 6e) and 6f), respectively. In addition, in all these figures the LO_1 and LO_2 pikes corresponding to covalent interactions with Cu^{2+} and Cu^{1+}, respectively [1,2], are shown. These spectra are related to the multivalent states of Cu_xO ($x = 1, 2, 3$) to determine the stoichiometry. The calculated data here represent a new associated contribution to crystallographic defects, although there is no experimental evidence of V_O in the crystal structure.

Reported Ab initio calculations for the oxygen, from an octahedral site coordination (O_h) [15,17,18], in this work, the A-NFs sample has the same coordination, in agree with the CTM4XAS study showed in Refs. [1,2,17]. In contrast, the B-NFS displayed a tetrahedral sites coordination and a more distorted lattice. We think that this distortion and the calculated distance shifts between the Cu and O in the structure by the Fullprof software, suggest a final state derives

as $2p^6 3d^9 \rightarrow 2p^5 3d^{10}$ Ref. [20,21]. This result agrees with those of both J. Coey, 2005 and F. De Groot, *et al*., 2016 who concluded that in the system there is a high- spin, suggesting magnetic effects, as we deduced too from our outcomes [20,21].

3.4. Magnetic analysis

Figures 7a to 7d) presents the study of magnetization versus field, displaying hysteresis loops at 300 K indicative of ferromagnetic behavior. This behavior aligns with that observed in both pure CuO and Mn-doped CuO nanowires as reported by D. Han *et al*., 2016 [34]. The ferromagnetic properties are attributed to crystallite sizes and doping levels: 117 nm (8.0% Mn) as noted in reference [34], and 22 nm and 42 nm (3.0% Mn) [7]. Hysteresis loops for nanofibers at 300 K reveal coercive fields H_C of 0.24 kOe (A-NFs) and 0.006 kOe (B-NFs). Studies by R. Narsinga Rao *et al*., in 2009 and 2005, and R. Borzi *et al*., identified an H_C of 0.20 kOe in nanoparticles. D. Han *et al*., in 2016, also observed similar behavior at low temperatures (60 K) in CuO nanowires doped with 15.0% and 8.0% Mn, reporting H_C values of 0.50 kOe. In Fig. 7e) illustrates magnetic susceptibility with respect to temperature, reflecting a paramagnetic behavior, which suggests, according to Ref. [7], that the area-volume relationship is dominant and indicative of structural disorder. Furthermore, the inverse of the susceptibility [Fig. 7f)] is plotted to confirm the antiferromagnetic (AFM) nature of these materials. G. Narsinga Rao *et al*., in studies conducted in 2005 and 2009, examined the AFM phase of commercial CuO (500 nm) [5,6] compared to nanoparticles ranging from 13 nm to 33 nm, demonstrating such a phase at approximately 230 K.

4. Conclusions

CuO, and 3% Mn doped CuO nanofibers were successfully synthetized by of electrospinning method. The doped material showed an increase of diameter and a decrease of microdeformations. The XRD experimental spectra allowed verify the presence of Tenorite phase for both materials.

From the calculated results by VESTA software for the B-NFs, mainly in the electron density calculation exhibited the existence of a bond of covalent nature, as well as approaching displacements between Cu-Cu in the (001) plane and Cu-O in the (110) plane, in the doped nanofibers, with respect to A-NFs. These displacements have been linked to paramagnetism behavior [27, 32] in agree with our result [7].

An interesting structural result for the chemical coordination modification refers to a notable shift between the octahedral site coordination for A-NFs and the tetrahedral site coordination for B-NFs. We attributed this phenomenon to Jahn-Teller effect. These results agree with those predicted by VESTA, about charge transference between Cu and O that deforms the structure, generating the Jahn-Teller effect too.

The binding energy shifts between the Cu 2p3/2 and Cu 2p1/2, in the B-NFs spectrum, suggest a paramagnetic contribution, due to a charge decompensation.

The magnetic study in the NFs revealed paramagnetic behavior at low temperatures and ferromagnetism at room temperature, attributable to the area-volume relationship. Moreover, the observed ferromagnetic behavior is linked to the size and shape of the materials. In this case of the Mn doped materials, the behavior is further associated with the superexchange interaction between the Cu d orbital and the Mn $2p$ and Cu $2p$ orbitals, facilitated by the latter being half-filled.

Acknowledgments

The authors acknowledge the support of CONAHCYT scholarship grants No. 467043 and Irving Adrian Prieto-Gómez's support in typewriting this paper.

Data Availability Statement:

The data in my manuscript can be obtained from the corresponding author.

Conflicts of Interest:

The authors declare no conflict of interest.

1. M. B. K. *et al*, Binary copper oxide semiconductors: From materials towards devices, *Phys. status solidi*, **249** (2012) 1487, https://doi.org/10.1002/pssb.201248128.

2. N. M. Basith, J. J. Vijaya, L. J. Kennedy, and M. Bououdina, Structural, morphological, optical, and magnetic properties of Ni-doped CuO nanostructures prepared by a rapid microwave combustion method, *Mater. Sci. Semicond. Process.* **17** (2014) 110, https://doi.org/10.1016/J.MSSP.2013.09.013.

3. A. Rahnama and M. Gharagozlou, Preparation and properties of semiconductor CuO nanoparticles via a simple precipitation method at different reaction temperatures, *Opt. Quantum Electron.* **44** (2012) 313, https://doi.org/10.1007/s11082-011-9540-1.

4. R. A. Borzi, S. J. Stewart, R. C. Mercader, G. Punte, and F. Garcia, Magnetic behavior of nanosized cupric oxide, *J. Magn. Magn. Mater.*, **226-230** (2001) 1513, https://doi.org/10.1016/S0304-8853(00)00943-4.

5. G. N. Rao, Y. D. Yao, and J. W. Chen, Superparamagnetic behavior of antiferromagnetic CuO nanoparticles, *IEEE Trans. Magn.,* **41** (2005) 3409, https://doi.org/10.1109/TMAG.2005.855214.

6. G. Narsinga Rao, Y. D. Yao, and J. W. Chen, Evolution of size, morphology, and magnetic properties of CuO nanoparti-

cles by thermal annealing, *J. Appl. Phys.,* **105** (2009) https://doi.org/10.1063/1.3120785.

7. M. Piñón-Espitia, M. A. Garza-Navarro, and M. T. Ochoa-Lara, Superparamagnetism in pure and Mn-doped CuO nanofibers, originated by oxygen vacances, *Microsc. Microanal.,* **27** (2021) 1782, https://doi.org/10.1017/s1431927621006528.
8. T. H. Tran and V. T. Nguyen, Copper Oxide Nanomaterials Prepared by Solution Methods, Some Properties, and Potential Applications: A Brief Review, *Int. Sch. Res. Not.,* **2014** (2014) 1, https://doi.org/10.1155/2014/856592.
9. D. Gao, G. Yang, J. Li, J. Zhang, J. Zhang, and D. Xue, Room-Temperature Ferromagnetism of Flowerlike CuO Nanostructures, https://doi.org/10.1021/jp106015t.
10. R. N. Mariammal, K. Ramachandran, G. Kalaiselvan, S. Arumugam, B. Renganathan, and D. Sastikumar, Effect of magnetism on the ethanol sensitivity of undoped and Mn-doped CuO nanoflakes, *Appl. Surf. Sci.,* **270** (2013) 545, https://doi.org/10.1016/j.apsusc.2013.01.084.
11. J. M. D. Coey, Chapter 19 Magnetism of Dilute Oxides, *Springer* **678** (2005) 185, https://doi.org/10.1007/11417255_12.
12. M. U. Delgado-Jaime, K. Zhang, J. Vura-Weis, and F. M. F. De Groot, CTM4DOC: Electronic structure analysis from X-ray spectroscopy, *J. Synchrotron Radiat.,* **23** (2016) 1264, https://doi.org/10.1107/S1600577516012443
13. M. T. O.-L. M. Piñón-Espitia, D. Lardizabal-Gutiérrez, M.L. Camacho-Ríos, G. Herrera-Pérez, Electronic structure comparison of Cu_2p and O 1s X-Ray photoelectron spectra for Cu x O nanofibers ($x = 1, 2,$ i), *Mater. Chem. Phys.*, **272** (2021) 124980, https://doi.org/10.1016/j.matchemphys.2021.124981.
14. M. Piñón-Espitia, D. Lardizabal-Gutiérrez, M. L. Camacho-Ríos, G. Herrera-Pérez, A. Duarte-Moller, and M. T. Ochoa-Lara, Charge transfer effects and O2- vacancies in pure CuO nanofibers and enriched with 3.0% Mn, *Mater. Chem. Phys.*, **295** (2022) 126989, https://doi.org/10.1016/j.matchemphys.2022.126989.
15. K. Okada and A. Kotani, Multilet structure in Core-level XPS of High-Tc Material La2CuO4 and Related Cu - Compounds, *J. Electron Spectrosc. Relat. Phenom.,* **52** (1990) 313, https://doi.org/10.1016/0368-2048(90)85028-8.
16. OriginLab Corporation, Origin(Pro). Northampton, MA. USA, (2019).
17. T. Mizoguchi, I. Tanaka, S. P. Gao, and C. J. Pickard, First-principles calculation of spectral features, chemical shift and absolute threshold of ELNES and XANES using a plane wave pseudopotential method, *J. Phys. Condens. Matter,* **21** (2009) 104204, https://doi.org/10.1088/0953-8984/21/10/104204.
18. E. Stavitski and F. M. F. De Groot, Author's personal copy The CTM4XAS program for EELS and XAS spectral shape analysis of transition metal L edges, *Micron,* **41** (2010) 687, https://www.elsevier.com/copyright.
19. S. Åsbrink and L. J. Norrby, A refinement of the crystal structure of copper(II) oxide with a discussion of some exceptional e.s.d.'s *Acta Crystallogr. Sect. B Struct. Crystallogr. Cryst. Chem.,* **26** (1970) 8, https://doi.org/10.1107/s0567740870001838
20. J. Ghijsen, L. H. Tjeng, H. Eskes, G. A. Sawatzky, and R. L. Johnson, Resonant photoemission study of the electronic structure of Cuo and Cu_20 **42** (1990) 2017, https://journals.aps.org/prb/pdf/10.1103/PhysRevB.42.2268
21. J. I. Langford and D. Lou, Reports on Progress in Physics Related content Powder diffraction Powder diffraction, (1996).
22. V. V. Mesilov et al., X-ray Diffraction and X-ray Spectroscopy Studies of Cobalt-Doped Anatase TiO2:Co Nanopowders, *J. Phys. Chem. C,* **121** (2017) 24235, https://doi.org/10.1021/acs.jpcc.7b05873.
23. A. Amirsalari, A. Abdolahzadeh Ziabari, R. Taheri Ghahrizjani, and S. Farjami Shayesteh, A fundamental study on the effects of nano-silver incorporation on the structure and luminescence properties of color centers in γ'-alumina nanoparticles, *J. Lumin.,* **192** (2017) 910, https://doi.org/10.1016/j.jlumin.2017.08.011.
24. J. Salas-Leiva, G. Herrera-Pérez, L. Palma-Cano, G. Rojas-George, C. Ornelas-Gutierrez, and A. Luna-Velasco, Structural and Microstructural Analysis for CuO Nanoparticles Prepared by Precipitation Method., *Microsc. Microanal.*, **25** (2019) 1984, https://doi.org/10.1017/s1431927619010651.
25. E. A. Sanches, J. C. Soares, A. C. Mafud, E. G. R. Fernandes, F. L. Leite, and Y. P. Mascarenhas, Structural characterization of Chloride Salt of conducting polyaniline obtained by XRD, SAXD, SAXS and SEM, *J. Mol. Struct.,* **1036** (2013) 121 https://doi.org/10.1016/j.molstruc.2012.09.084.
26. F. Grasset *et al*., Surface modification of zinc oxide nanoparticles by aminopropyltriethoxysilane, *J. Alloys Compd.,* **360** (2003) 298, https://doi.org/10.1016/S0925-8388(03)00371-2.
27. H. Qin, Z. Zhang, X. Liu, Y. Zhang, and J. Hu, Room-temperature ferromagnetism in CuO sol-gel powders and films, *J. Magn. Magn. Mater.,* **322** (2010) 1994, https://doi.org/10.1016/j.jmmm.2010.01.021.
28. R. A. Borzi, S. J. Stewart, R. C. Mercader, G. Punte, and F. Garcia, *Magnetic behavior of nanosized cupric oxide* **230** (2001) 1513, https://doi.org/10.1016/S0304-8853(00)00943-4.
29. H. Cao, Z. Zhou, J. Yu, and X. Zhou, DFT study on structural, electronic, and optical properties of cubic and monoclinic CuO, *J. Comput. Electron.,* **17** (2018) 21, https://doi.org/10.1007/s10825-017-1057-9.
30. G. Herrera-Perez, J. Plaisier, A. Reyes-Rojas, and L. Fuentes-Cobas, Â´Â´Electron density contour maps via Rietveld-MEM analysis using HR-XRD for the polycrystalline ferroelectric BCZT, *Supl. Rev. Mex. Fis* **3** (2022) 1-6, https://doi.org/10.31349/suplrevmexfis.3.010601.
31. Z. Cvejic et al., Influence of heavy rare earth ions substitution on microstructure and magnetism of nanocrystalline magnetite, *J. Alloys Compd.,* **472** (2009) 571, https://doi.org/10.1016/j.jallcom.2008.05.026.
32. J. M. D. Coey, doi:10.1016/j.cossms.2006.12.002, https://doi.org/10.1016/j.cossms.2006.12.002.

33. A. Sabirin Zoolfakar, R. A. Rani, A. J. Morfa, A. P. O'mullane, and K. Kalantar-Zadeh, Nanostructured Copper Oxide Semiconductors: a Perspective on Materials, Synthesis methods and Applications, *J. Name,* **00** (2013) 1-3, https://doi.org/10.1039/x0xx00000x.